CrossMark

The Baryonic Tully–Fisher Relation. II. Stellar Mass Models

Francis Duey[1] , James Schombert[2] , Stacy McGaugh[1] , and Federico Lelli[3]

[1] Department of Astronomy, Case Western Reserve University, Cleveland, OH 44106, USA
[2] Department of Physics, University of Oregon, Eugene, OR 97403, USA
[3] Arcetri Astrophysical Observatory (INAF), Florence, Tuscany, Italy

Abstract

We present new color–Υ_* (mass-to-light ratio) models to convert Wide-field Infrared Survey Explorer W1 fluxes into stellar masses. We outline a range of possible star formation histories and chemical evolution scenarios to explore the confidence limits of stellar population models on the value of Υ_*. We conclude that the greatest uncertainties (around 0.1 dex in Υ_*) occur for the bluest galaxies with the strongest variation in recent star formation. For high-mass galaxies, the greatest uncertainty arises from the proper treatment of bulge–disk separation in which to apply different Υ_* relations appropriate for those differing underlying stellar populations. We compare our deduced stellar masses with those deduced from Spitzer Space Telescope 3.6 μm fluxes and stellar mass estimates in the literature using optical photometry and different Υ_* modeling. We find the correspondence to be excellent, arguing that rest-frame near-IR photometry is still more advantageous than other wavelengths.

Unified Astronomy Thesaurus concepts: Galaxy photometry (611)

Materials only available in the online version of record: *machine-readable table*

1. Introduction

The conversion of stellar luminosity into stellar mass is the keystone to understanding the total baryonic mass of a galaxy (B. M. Tinsley 1968) and its mass distribution (H. J. Ibarra-Medel et al. 2022). In addition, the stellar mass of a galaxy is the primary output of its star formation history (SFH), the conversion of neutral gas into stars, and the defining characteristic for the evolution of the galaxy (J. S. Speagle et al. 2014). The production, or lack of production, of stars defines a galaxy's morphology (P. Cassata et al. 2007), color evolution (K. D. Rakos & J. M. Schombert 1995), and metallicity evolution (W. M. Baker et al. 2023). Whether the growth of stellar mass happens in a monolithic (O. J. Eggen et al. 1962) or hierarchical fashion (T. Treu et al. 2005), our understanding of the baryon cycle begins with the galaxy's current stellar mass.

The path to determining stellar mass begins with photometry, as the luminosity of a galaxy is simply a proxy for the number of stars. The photometry of galaxies has a long history (M. M. Roth et al. 2023) stretching from uncalibrated photographic imaging through the era of photoelectric photometry that produced catalogs such as the Third Reference Catalogue (G. de Vaucouleurs et al. 1991) to the present-day digital sky surveys from the ground (e.g., the Sloan Digital Sky Survey (SDSS); G. Consolandi et al. 2016) and space (e.g., the Wide-field Infrared Survey Explorer (WISE); E. L. Wright et al. 2010). However, even for an isolated galaxy with few nearby stellar sources, the determination of an accurate flux (total or by area, i.e., surface photometry) is an observational challenge (D. W. Hogg 2022). An additional dilemma arises with any attempt to extract a true bolometric flux from photometric magnitudes without some knowledge of the total

energy flux emitted across all wavelengths (M. J. I. Brown et al. 2014).

As noted by E. N. Taylor et al. (2011), almost all the characteristics of a galaxy, including its morphological appearance, vary sharply during the course of its evolution. Detailed analysis of the color–magnitude diagrams of stellar populations in nearby galaxies (D. R. Weisz et al. 2011) shows that the SFH of a galaxy may change dramatically, often on short timescales, along with its color and mean parameters such as stellar population age and metallicity. The global properties of galaxies, including their kinematics, are well correlated with their total stellar masses, regardless of their suspected paths of galaxy evolution (see I. Strateva et al. 2001; A. Gallazzi et al. 2006). The exploration of these stellar mass scaling relations back to the era of galaxy formation is a primary science goal of the recently launched James Webb Space Telescope (A. Dressler et al. 2023).

The process of converting galaxy fluxes into stellar mass requires interpretation with a stellar population model. These models take a unit amount of gas mass and an initial mass function, plus an assumed SFH and chemical enrichment scenario, and combine these functions with known stellar isochrones to produce a mean mass-to-light ratio (Υ_*). The effects of age and metallicity on the Υ_* of stellar populations are obvious from even the simplest star formation scenarios. For example, a young stellar population rich in high-mass O stars will have a particularly low Υ_* due to the enormous luminosity of O stars as compared to an old stellar population dominated by lower-luminosity red giant branch stars, which will drive Υ_* to higher values (B. M. Tinsley 1978).

At the core of these population models are the simple stellar populations (SSPs), stellar groups of single age and metallicity (A. G. Bruzual 1993). While the colors and spectral energy distributions (SEDs) of SSPs are well matched to the observations of compact systems, such as globular clusters, they fail to adequately match the colors of normal galaxies due to the complex mixing of many populations of different ages

and metallicities (B. M. Tinsley 1980). A real, present-day galaxy will have a stellar population that evolved over time in two basic ways, (1) a changing star formation rate (SFR; i.e., the SFH) plus (2) a growing mean metallicity as previous generations have enriched the interstellar medium from which the next generation of stars form (chemical evolution). Basic composite stellar populations (CSPs), ones which are linear combinations of SSPs, produce high-quality matches to the color and spectroscopic characteristics of normal galaxies (E. F. Bell et al. 2003; A. Gallazzi et al. 2005) and provide a testable pathway to mapping Υ_* onto observables such as morphological type or mean color (J. Walcher et al. 2011; SML).

An additional level of accuracy is obtained when CSP models are matched to the galaxy observables such as a full SED, various spectral indices, or widely spaced colors to limit the range of properties of the underlying stars. Each technique has its various strengths and inherent uncertainties. For example, one of the finest analyses comparing synthetic SEDs to multiband photometry is the GAMA project (S. P. Driver et al. 2009) outlined in detail in E. N. Taylor et al. (2011). Their technique of fitting the flux in nine bandpasses from the UV to the near-IR produces uncertainties in stellar mass of only 0.12 dex (28%). While they conclude that the addition of mid-IR fluxes adds additional uncertainty, probably due to the luminosity changes induced by short-lived asymptotic giant branch (AGB) stars, they found acceptable errors when just using SDSS fluxes and a $g - i$ color relation to deduce an Υ_*.

This is the second paper in our series to study one of the key galaxy scaling relations, the baryonic Tully–Fisher (TF) relation. We have dedicated this paper to the construction of an observational technique for the conversion from flux densities (centered on the WISE mission photometric archives) to stellar mass, which, when combined with the gas mass, becomes the total baryonic mass of the galaxy. Our first paper in this series (F. Duey et al. 2023) outlined our procedures and protocols for using WISE and Spitzer Space Telescope (Spitzer) imaging to assign a total galaxy luminosity. The goal of this paper is to (1) introduce new mass-to-light models for the WISE filters, (2) compare these models to Spitzer and SDSS stellar masses, and (3) map the resulting luminosity TF relation into the stellar mass TF, popular in distance scale studies (R. B. Tully et al. 2009). The third paper in this series will be to take the baryon masses deduced in Papers I and II, combined with redshift-independent distances, to definitively characterize the IR baryonic TF relation in order to explore the kinematic scaling relations of disk galaxies and standardize the baryonic TF for distance scale work.

2. WISE Mass-to-light Models

For stellar mass determination, the near-IR offers a portion of a galaxy's spectrum that is dominated by starlight free from strong emission lines and with limited changes due to young stars. In addition, the low Galactic and internal extinction corrections make near-IR fluxes more consistent across morphological types. The SPARC project depended on pointed observations from Spitzer (M. W. Werner et al. 2004). With the termination of the Spitzer mission, future dynamical studies from our team will use the all-sky data set from the WISE mission (E. L. Wright et al. 2010). Fortunately, the WISE and Spitzer filters overlap in the near-IR.

The last step to converting a luminosity to a stellar mass is an accurate mass-to-light ratio, Υ_*. The mass and luminosity of a single star is a straightforward calculation deduced from the field of stellar structure and has been calibrated with binary stars. The determination of the mass of a star cluster is also a well-solved problem if the age and metallicity of the stellar population is known (by, for example, matching isochrones to the cluster color–magnitude diagram). The integrated mass of an SSP can be deduced from the application of computed stellar evolutionary tracks and an assumed initial mass function, both of which can be tested by detailed color–magnitude diagrams (see M. W. Hosek et al. 2020) and various secondary spectral indices (see S. C. Trager et al. 1998). The procedure becomes much more complicated in the case of a late-type galaxy's stellar population, which will be composed of many different stars of varying ages and metallicities. A composite CSP requires some knowledge of the SFH of the galaxy (to assign an SSP at each time step) and a chemical enrichment model (to assign a metallicity to each generation; see J. H. Lee et al. 2023).

Two advances in recent years have dramatically improved our ability to deduce stellar mass from photometry for galaxies. The first is the increased sophistication in the suite of stellar isochrones used to produce stellar population models that allows inspection of the effects of exotic components, such as horizontal branch and blue straggler stars, as well as a more detailed understanding of the effects of dust and the initial mass function (see C. Conroy & J. E. Gunn 2010, hereafter CG10). In addition, there is an awareness that detailed SED fitting is not critical to deducing Υ_* from population models, so that broadband photometry can be adequate (A. Gallazzi & E. F. Bell 2009) as long as sufficient wavelength coverage is obtained. With this technique, one determines Υ_* through various mass-to-light versus color relations as well as from detailed spectral indices, a procedure that is still laced with complications (see S. S. McGaugh & J. M. Schombert 2014). One clear result from these photometric studies is that the dynamic range of Υ_* becomes narrower with increasing wavelength; however, beyond 4 μm the effects of hot dust decouple the photometry from stellar atmospheric luminosities and limit the ability to deduce Υ_*.

Our study follows the procedures described in J. Schombert et al. (2022 hereafter SML), which builds on the techniques focused on the near-IR filters developed in J. M. Schombert & S. McGaugh (2014). For the reasons stated above, and outlined in J. M. Schombert & S. McGaugh (2014), the optimal wavelength to deduce Υ_* is between 1 and 4 μm, i.e., photometry from the near-IR filters of *JHK* plus the regions covered by WISE W1 and Spitzer (IRAC 3.6 μm). Other studies (e.g., E. N. Taylor et al. 2011) have focused on full SED fitting from the UV to the far-IR. This has the advantage of being able to follow recent star formation plus a broader section of the SFH of a galaxy (with various optical filters being sensitive to varying and shorter timescales), but has the disadvantage of working with fluxes at wavelengths where the dust extinction is large and the Υ_* has a large dynamic range such that small errors in the photometry produce large uncertainties in Υ_*. E. N. Taylor et al. (2011) conclude that the use of near-IR photometry increases the uncertainty in the Υ_* value from full SED fits. SML reached a similar conclusion, but found fault was not in the near-IR fluxes but rather the stellar population models in the near-IR (see also

S. S. McGaugh & J. M. Schombert 2014). The model uncertainties developed from inadequate treatment of the AGB population and, therefore, SML used an empirical scheme to link the stellar population models to the K, W1, and IRAC 3.6 μm filters.

Our stellar population models are based on two main assumed functions, the SFH and the chemical evolution as a function of time. Our SFH scenarios (SFR as a function of age) fall into two classes: (1) the exponentially declining star-forming models outlined in J. S. Speagle et al. (2014) for galaxies with stellar masses greater than 10^{10} $M_\odot$ and (2) a slowly declining, nearly constant star-forming model to match the characteristics of the main sequence for galaxies with less than 10^{10} $M_\odot$. All the models assume an initial epoch of star formation of 12 Gyr ago (z_f between eight and 12) followed by a rapid burst which declines or levels off by 4 Gyr (see Figure 1 in SML). The age–metallicity relation follows the scenario proposed by N. Prantzos (2009) starting with a preenriched population of [Fe/H] = -1.5 followed by a rapid rise to 80% of the final metallicity (given by the mass–metallicity relation). Using these SFH and metallicity prescriptions, one can combine various SSPs to reproduce both the main sequence (SFR versus galaxy stellar mass) and the present-day two-color diagrams, the observational constraints on the modeling (see SML).

The uncertainty in these SFH models can be compared to the range in SFRs from the main sequence (S. S. McGaugh et al. 2017) and the scatter in galaxy color from the ridgelines in the two-color diagrams. Numerical experiments changing the SFR and metallicity growth by 30% or varying epochs of quasi-steady bursts, can recover the scatter in the main sequence and two-color diagrams (both measures of the present-day state of a galaxy's stellar population). These effects are important in two realms, the optical portion of the spectrum, which is sensitive to the short-lived components of a stellar population, and for low-mass dwarf galaxies, where there is already evidence that their SFHs are sporadic (see Hubble Space Telescope color–magnitude diagrams; D. R. Weisz et al. 2011). However, it is important to note that the integrated properties of galaxies are surprisingly narrow and coherent. Relationships, like the main sequence and the mass–metallicity relation, indicate that, even if the star formation path in late-type galaxies is erratic, ultimately they end up with a constant percentage of gas converted into stars at a relatively steady rate. This produces a final stellar population of similar distributions in age and metallicity in proportion to the total stellar mass. This is another reason for focusing on near-IR fluxes to determine stellar mass as those wavelengths are most sensitive to the stable, long-lived portions of a stellar population, minimally effected by dust extinction from recent star formation, and have the smallest percentage change in Υ_* in models with varying SFHs.

The most important component for the near-IR stellar populations is the treatment of thermally pulsating AGB stars. These are stars in the very late stages of their evolution powered by a helium-burning shell that is highly unstable. AGB stars have high initial masses ($M > 5$ $M_\odot$) and are intermediate in age ($\tau > 10^8$ yr). While the G. Bruzual & S. Charlot (2003 hereafter, BC03) codes (and their extension, see A. G. Bruzual 2009) include AGB stars as part of their evolutionary sequence, comparison with other codes (e.g., C. Maraston 2005; V. Gonzalez-Perez et al. 2014) finds

discrepancies in the amount of luminosity from this short-lived population. The history of AGB treatment in SED codes is outlined in CG10, and the work of M. Salaris et al. (2014) outlines the difficulty in AGB modeling, primarily due to (1) variations of brightness and color on timescales of a few thousand years, (2) their cool temperatures that have a dominant effect mostly in the near-IR (where spectral libraries are less complete), and (3) the formation of dusty envelope. All these factors significantly complicated the SED calculations. This is most certainly the origin of the disagreement between population characteristics deduced by E. N. Taylor et al. (2011) for optical versus near-IR colors.

Due to these complications, we have adopted a more empirical approach to the AGB component. As noted in J. M. Schombert (2016) and J. M. Schombert & S. McGaugh (2014), all the recent stellar population models were poor matches to the near-IR colors of populations younger than a few gigayears. To best determine which stellar population model matches our empirical AGB prescription, we compared extensions of the BC03 and CG10 models to the near-IR colors of LMC, SMC, and Milky Way star clusters. As metallicity typically decreases for older star clusters, it is problematic to compare a single metallicity SSP track to the colors versus age diagram. However, a solar metallicity model accurately captures the young cluster colors and conforms to a majority of the expected metallicity of stars in normal galaxies. There is very little difference between the solar BC03 and CG10 tracks, although adding a standard AGB dust model (A. Villaume et al. 2015) compares more favorably with the redder young cluster colors. We found the variation in metallicity is only important for very young and very old clusters (see Figure 6 in J. Schombert et al. 2019). As the timescales for these types of stars are short, their effects are most important for the last generation of stars in a galaxy, where the metallicity has reached its highest value by galaxy mass. This confines the range of AGB tracks required to reproduce near-IR fluxes.

Using these 116 star clusters, we tabulate a set of $V - K$ colors for a range of age and metallicities, which we apply to our stellar population algorithm that builds a composite population with a selected SFH and chemical enrichment scenario (see SML). For IRAC 3.6 μm fluxes, we built empirical $K - [3.6]$ versus $V - K$ or $g - K$ color relations using S^{4}G (K. Sheth et al. 2010) and SPARC samples. We apply these relationships to the K population models to calculate Υ_* at 3.6 μm. A reality check is provided by the fact the stellar population models correctly predict the various optical to 3.6 μm colors over a range of star formation and chemical evolution scenarios.

Lastly, we perform the same operations for this paper on the W1 filter set, using the color relations outlined in Paper I. Our final Υ_* diagrams are shown in Figure 1. Differing from our previous papers, we present the Υ_* color relations using SDSS g and W1 rather than $V - [3.6]$. The difference from $V - [3.6]$ to $g - [3.6]$ is small, and either color or morphological type is equally suitable for deducing Υ_* (see Figure 2 from SML). The trends in Figure 1 are similar to previous color–Υ_* studies, showing a sharp difference between star-forming and passive galaxy populations (disk versus bulge) and a steady, rising Υ_* with redder color. The short decrease in Υ_* for blue colors is a distinct feature of the medium-aged AGB stars dominating the near-IR fluxes in high-SFR regions; a similar feature is seen in the optical from high-mass OB versus A stars. While we have
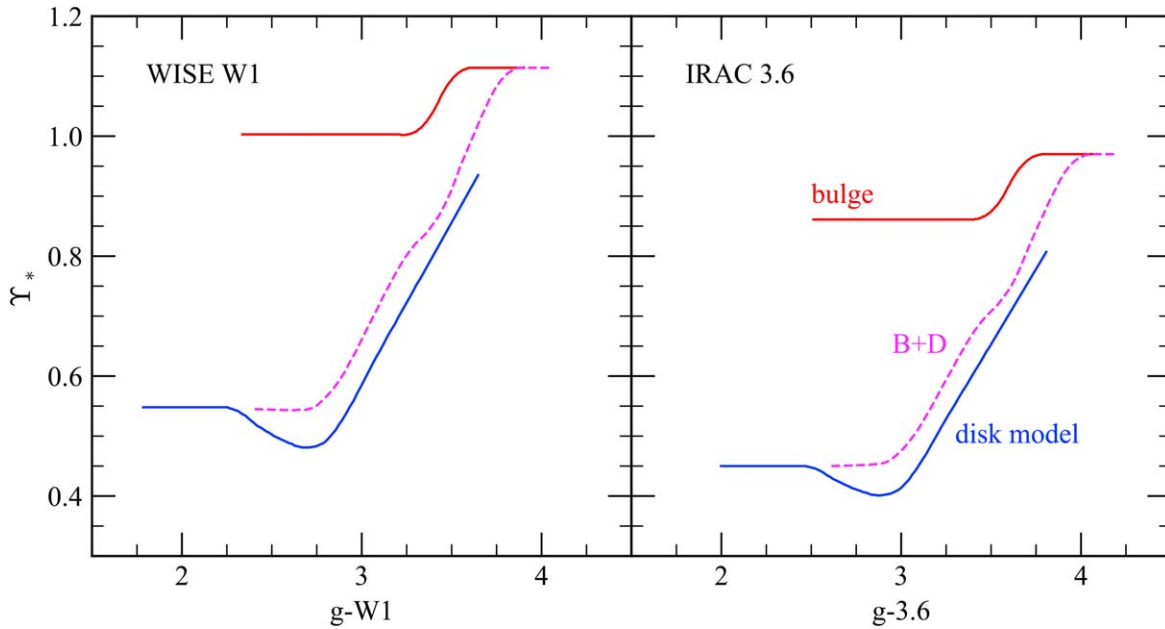
Figure 1. Updated Υ_* models from SML. The three models shown (discussed in the main text) represent pure bulge and disk SFHs, which are then combined to produce a bulge + disk ("B + D") scenario guided by the main-sequence relation (J. S. Speagle et al. 2014) and a chemical enrichment model. Standardized to the $g - W1$ or $g - [3.6]$ color, at the 3.5 μm wavelength the difference between Υ_* is only larger by 10% from IRAC 3.6 μm to WISE W1.

displayed our declining star-forming models, a constant or enhanced SFR will significantly alter the blue end of the color–Υ_* relation by ±0.08 dex (see Figure 2 in SML) even in the near-IR.

Three Υ_* scenarios are shown in Figure 1: a pure bulge model, a pure disk model, and a hybrid bulge + disk model. Both the bulge and disk models are based on a simplistic interpretation of either a uniform, old stellar population (bulge) or a young, star-forming (i.e., dominated by massive stars) stellar population (disk). Variation in color for the bulge scenario is due to increasing the mean metallicity of the stars from $[Fe/H] = -1.5$ to supersolar. The jump near $g - W1 = 3.3$ is due to a sudden drop in the luminosity of AGB stars at near-solar metallicities, confirmed by the color of high-mass ellipticals. For the star-forming disk scenario, the rise in Υ_* with color is a combination of stronger star formation (J. S. Speagle et al. 2014) with high-mass galaxies (i.e., more star formation in the past and redder present-day colors) and higher final metallicities (G. Cresci et al. 2019). These models, for a range of metallicities and SFHs, can be found at the SPARC website at http://astroweb.cwru.edu/SPARC/.

The bulge and disk models were produced in order to be applied to particular portions of a galaxy's luminosity profile to give a combined spatial and luminosity weight to a deduced value of Υ_*. However, many galaxy surveys have limited spatial resolution (particularly at high redshift), and these data sets frequently only offer a total luminosity value. In order to more accurately produce a total stellar mass from a total luminosity, we used the fact that the color and morphology of galaxies are strongly correlated, and that relationship, in part, reflects the correlation of bulge-to-disk (B/D) ratio with color. A hybrid bulge + disk model is produced by combining the stellar populations from the pure bulge and disk models as a function of the B/D ratio, plotted against color. Unsurprisingly, increasing B/D also reflects into redder colors (A. W. Graham & C. C. Worley 2008) and, to first order, one could substitute morphological type in the place of $g - W1$ color and produce

roughly the same Υ_* (to ±10%). The bulge + disk models are shown in Figure 1 and notice the obvious behavior on the blue side where late-type galaxies with small or nonexistent bulges converge on the pure disk model. Likewise, the early-type galaxies with high B/D ratios merge into the pure bulge scenario and the presence of even a small bulge in Sc-type galaxies allows a monotonic connection from early- to late-type systems.

3. Comparison of WISE Conversion to Stellar Mass

Central to our technique is the use of color as a proxy for the metallicity and mean stellar age to deduce Υ_*. As outlined in SML (see their Figure 9), the mass–metallicity and mass–SFR relationships are sufficiently narrow to limit the range in the characteristics of the underlying stellar population and predict a fairly well-defined Υ_* versus color relation. This has been demonstrated by several authors in the optical (E. F. Bell & R. S. de Jong 2000; E. N. Taylor et al. 2011) and in the near-IR (M. Eskew et al. 2012; S. E. Meidt et al. 2014) but is highly dependent on the smooth, coherent evolution of galaxy stellar populations. And there is every expectation that the uncertainty in the models grows with decreasing galaxy mass as their SFH becomes more erratic (D. R. Weisz et al. 2011).

Our Υ_* models are based on optical to near-IR colors, confined by our optical versus near-IR two-color diagrams. However, an alternative scheme to use W1 − W2 colors produces similar results. The WISE study from M. E. Cluver et al. (2014) showed that W1 − W2 is well correlated with log Υ_* deduced from GAMA stellar masses determined by SED fits from E. N. Taylor et al. (2011). While there were two distinct populations representing passive and star-forming galaxies, a linear trend was evident, and the maximum likelihood fit of log $\Upsilon_* = -1.96(W1 - W2) - 0.03$ was obtained (see their Figure 6).

We can use the WISE colors for the SPARC/WISE sample to compare the stellar masses inferred from our optical to near-
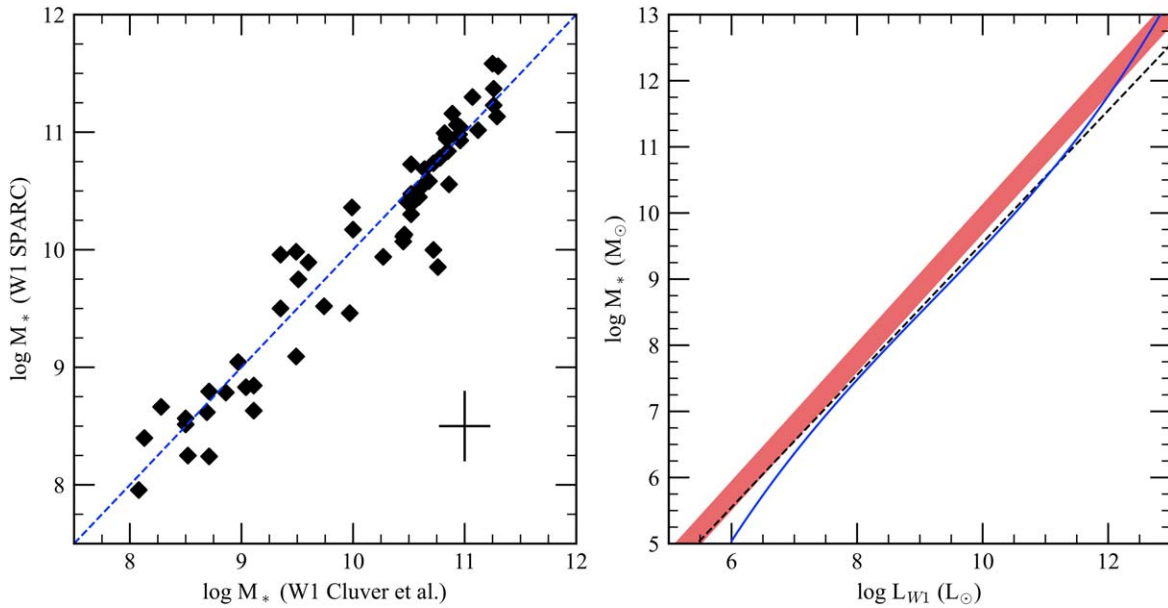
Figure 2. A comparison of stellar masses deduced by $g - W1$ colors (SPARC) vs. $W1 - W2$ color relation (M. E. Cluver et al. 2014). The WISE sample was selected for only those galaxies in the SPARC sample with W2 fluxes with a signal-to-noise ratio (S/N) greater than 20. Typical errors in the stellar mass are shown and the rms for the comparison of 58 galaxies is 0.29 in log scale. The right panel displays the log L_{W1} vs. stellar mass relationship outlined in T. H. Jarrett et al. (2023; magenta line, a polynomial fit to the GAMA masses). Our WISE models are shown as a red band of ± 0.2 dex error width based on a $g - W1$ color–magnitude relation to obtain L_{W1}. The dashed line indicates a constant $\Upsilon_* = 0.35$.

IR color technique to M. E. Cluver et al.'s (2014) WISE color technique. The results are shown in Figure 2, where we used a similar flux cutoff in signal-to-noise ratio (S/N) at W2 as M. E. Cluver et al. (2014) and used the mean errors in our fits to determine a mean error bar. As can be seen in Figure 2, the correspondence is excellent with a limiting rms between the sample of 58 galaxies of 0.29 in log scale. This may represent the limit on stellar mass calculations using different models and assumptions, but reinforces our earlier conclusion that optical- or near-IR-determined stellar masses are in agreement for low redshifts.

A different relationship between W1 fluxes and stellar mass is found by T. H. Jarrett et al. (2023). In that study an improved version of the GAMA stellar masses is used (GAMA-G23; A. S. G. Robotham et al. 2020) and new WISE total magnitudes from T. H. Jarrett et al. (2019). They follow a series of interlocking techniques to determine stellar mass such as a straightforward log L_{W1} versus log M_* relationship (a third-order polynomial, but very close to a linear relationship), a revised $W1 - W2$ color scheme, and a new $W1 - W3$ color relation. The $W1 - W2$ colors have the same range and mean as the SPARC sample, so our photometry is in agreement. However, our resulting stellar masses are about 0.2 dex higher than their total flux relation. This can be seen in the right panel of Figure 2, which shows the log L_{W1} relationship from T. H. Jarrett et al. (2023) fit in comparison to our Υ_* models where we use the $g - W1$ color–magnitude relation as a proxy for absolute luminosity, L_{W1}. A constant Υ_* value of 0.35 is shown to demonstrate the difference between our higher ($\Upsilon_* > 0.4$) values at low luminosities.

These new WISE stellar mass estimates from T. H. Jarrett et al. (2023) are difficult to reconcile with Υ_* values deduced for K and IRAC 3.6 μm. For example, the range in $K - [3.6]$ colors is between 0.1 and 0.4 (SML), which, when converted into solar luminosities, corresponds to a mean luminosity at K that is 1.5 times higher than [3.6] (these also correspond to the

observed SEDs; M. J. I. Brown et al. 2014). Our previous Υ_* models have a value of 0.45 at [3.6] for a late-type galaxy with a $K - [3.6]$ color of 0.3. The corresponding Υ_* for K is 0.6, which produces identical stellar masses from K and 3.6 μm luminosities (given the absolute magnitude of the Sun; C. N. A. Willmer 2018). Since the typical $W1 - [3.6]$ color for a late-type galaxy is 0.15, corresponding to a W1 flux in solar luminosities that is 12% fainter than at 3.6 μm (they have identical solar absolute magnitudes). Therefore, the expected Υ_* value should be near 0.5 for W1, in agreement with our models, but slightly higher than the value of 0.2 predicted by T. H. Jarrett et al. (2023). This may signal a systematic difference in our W1 fluxes (unlikely) or a systematic underestimate of near-IR Υ_* values from optically determined SED fits. In either case, this would also result in a sharp disconnect between stellar masses calculated from Spitzer luminosities compared to WISE, as will be explored in the next section.

Another avenue is to consider the change in the gas fraction produced by low Υ_* values. Following the analysis of F. Lelli et al. (2016), the gas fraction (M_{gas}/M_{bar}) is shown in Figure 3 as a function of galaxy W1 luminosity in solar units. Using our WISE Υ_* relationship based on galaxy color produces the data in the left panel. The gas fraction anticorrelates with luminosity in a predictable manner with Hubble type. One expects that early-type spirals, being gas-poor, bottom out at high luminosities, likewise gas-rich, late-type galaxies flatten out at low luminosities. An expected S-shaped change in gas fraction from early to late types is seen. This closely matches the predictions from Illustris-TNG50 galaxy formation simulations (M. Korsaga et al. 2023).

The lower Υ_* proposed by the GAMA-G23 stellar masses has the effect of raising the gas fractions for all galaxy types (although significantly for late-type dwarfs). Rather than an S-shaped progression from early to late types in terms of gas fraction, the resulting new relationship has more of a box-like
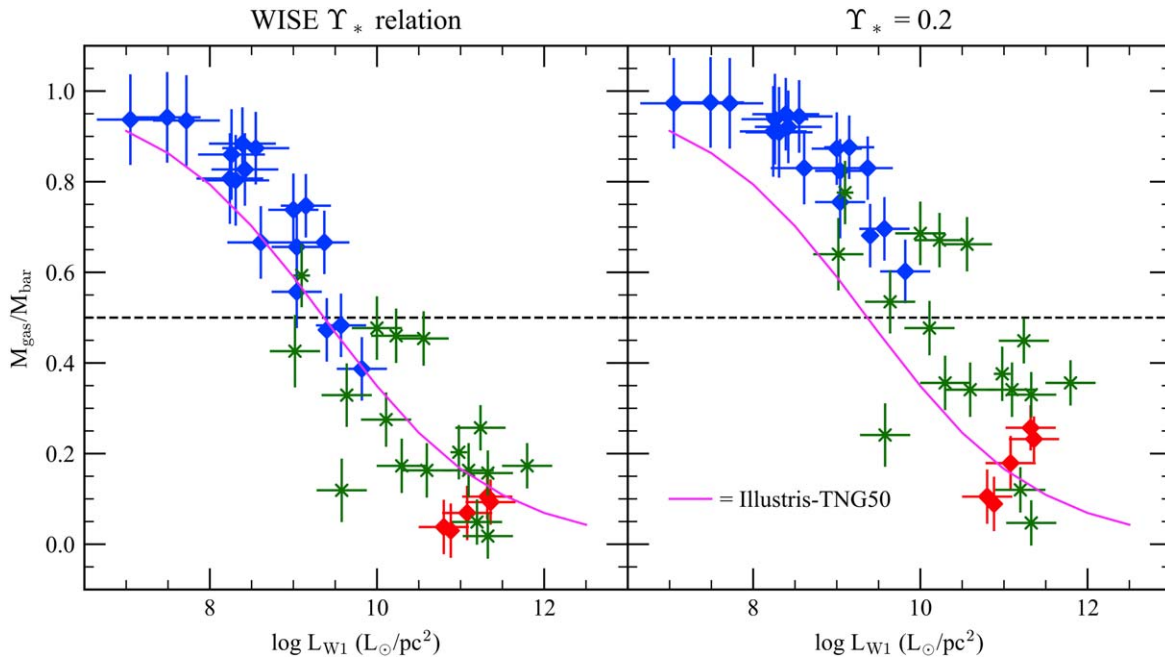
Figure 3. A comparison of W1 luminosity vs. gas fraction, M_{gas}/M_{bar}, for the WISE SPARC sample. The left panel displays gas fractions using the color relation presented in this paper, while the right panel uses a constant value of 0.2 proposed by T. H. Jarrett et al. (2023). Hubble types are indicated such that early-type spirals are red symbols, Sc's are green, and late-type dwarfs are blue. The prediction of gas fraction as a function of luminosity from the Illustris-TNG50 galaxy formation simulations (M. Korsaga et al. 2023) is shown as a magenta line.

shape, a sharp rise from Sa to Sc. In addition, over one-third of SPARC galaxies would have gas fractions above 0.5 (gas-dominated disks, dashed line; S. Courteau 1996) for $\Upsilon_* = 0.2$. This is very strange for spiral galaxies because density wave theory (C. C. Lin & F. H. Shu 1964) suggests that well-developed spiral patterns cannot be supported in heavily gas-dominated disks. In summary, low Υ_* values are difficult to reconcile with known gas and kinematic relationships for gas-rich galaxies.

4. Comparison of WISE to Spitzer Total Stellar Masses

While the same population models are used to deduce the stellar masses through the W1 or IRAC 3.6 μm filters, the calibrations depend on the accuracy of the photometry and interpretation of the color–color relations from Paper I. As discussed in SML, three different models can be used depending on the quality of the photometry. If the galaxy in question is fully resolved, then a bulge model can be used to assign a bulge stellar mass and a disk model can be applied to the star-forming region to assign a disk mass. The two components can be summed for a total stellar mass. If a full surface brightness profile is lacking, the B/D ratio can be estimated from the galaxy's color or morphological type (A. W. Graham & C. C. Worley 2008) and a combined model (labeled "B + D" in Figure 1) can be applied to the total luminosity of the galaxy. If using the total color, the model uses the B/D to color relationship from SML to deduce a B/D luminosity ratio and sum the resulting stellar from the arithmetic sum of the two components. As will be shown in the next paper of this series, this can have a significant impact on the deduced stellar masses of early-type spirals with their large B/D ratios.

As a check to our procedure, we use just the galaxy's $g - [3.6]$ or $g - W1$ color to assign an Υ_* for each galaxy in the SPARC sample with SDSS imaging. We use identical apertures for SDSS g, W1, and 3.6 μm in order to measure the same absolute fluxes (i.e., a metric color) and assign a comparable stellar mass. The resulting comparison stellar masses are shown in Figure 4 and the deduced stellar masses, colors, and Υ_* values are listed in Table 1. The correspondence is excellent with the relationship of unity well within the photometric errors. The few outliers all have higher stellar masses in W1, probably indicating that stellar contamination by foreground stars is still a serious concern for W1 photometry and can overestimate a galaxy's total luminosity without some visual inspection of the region around the WISE images.

In addition to a comparison with our own Spitzer photometry, we can also compare to stellar mass estimates in the literature. We have selected the S⁴G stellar masses (J. C. Muñoz-Mateos et al. 2015), which used the M. Eskew et al. (2012) technique for converting 3.6 μm fluxes into solar masses. There were 20 galaxies in common with the SPARC samples shown in red in Figure 4. Also selected were 16 galaxies in common with the Dustpedia survey (C. J. R. Clark et al. 2018), which used 42 filters from the Galaxy Evolution Explorer (GALEX) to the Atacama Large Millimeter/sub-millimeter Array to determine the stellar mass from SED fitting. Both samples are in excellent agreement with our W1 stellar masses. In particular, we note good agreement with the S⁴G sample, which used a different formula for determining Υ_*, but over the same portion of the spectrum as our W1 data. We also note that Dustpedia uses the full range of optical to mid-IR fluxes and a superior SED algorithm to determine Υ_*, yet achieves the same values as our IR technique.

5. Comparison of WISE to Spitzer Stellar Mass Densities

Total and aperture fluxes are the focus of the vast majority of stellar mass literature, and most of the stellar mass scaling relationships focus on integrated values. However, recent discoveries on the baryon–dark matter connection involve
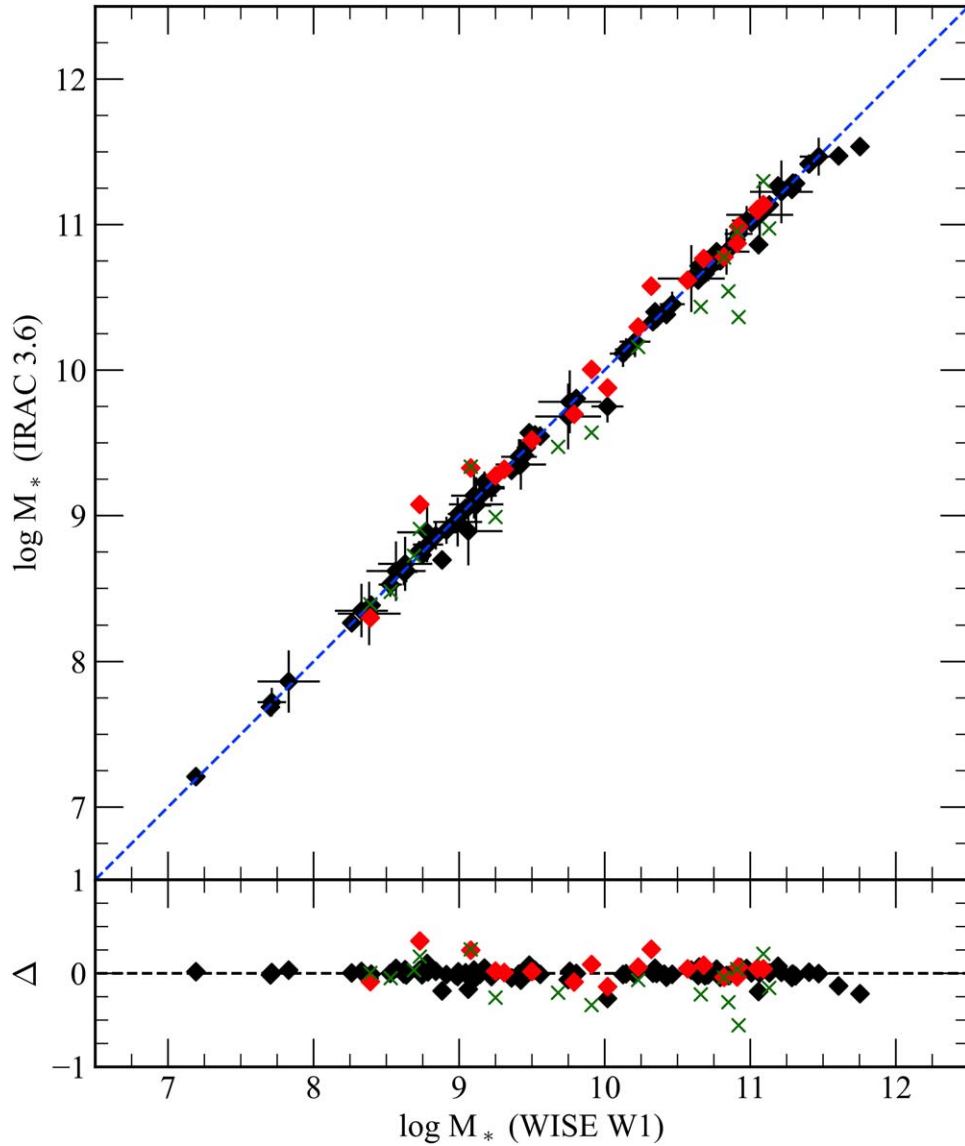
Figure 4. Using the models from Figure 1, the IRAC 3.6 μm and WISE W1 total luminosities are converted into total stellar masses in an independent fashion. Due to the typically redder and narrow range of W1 − [3.6] colors plus only slightly higher Υ_* values, it is unsurprising to find the relationship between stellar mass at W1 and 3.6 μm has a slope of 1. The error from a slope of unity is ±0.01 and the scatter is completely explained by photometric errors. The red and green symbols are 20 and 16 galaxies in common from the S^{4}G and Dustpedia surveys, respectively. The residual diagram at the bottom shows no systematics over the range of stellar masses with a mean offset of 0.02 ± 0.18 dex.

Table 1
WISE Stellar Masses

Name	$\log L_{W1}$ ($L_\odot$)	$\log M_{W1}$ ($M_\odot$)	$g - W1$	Υ_{W1}
LSBC F568-1	9.67	9.41 ± 0.06	2.50	0.55
LSBC F568-3	9.79	9.52 ± 0.03	2.73	0.54
LSBC F568-V1	9.44	9.17 ± 0.04	2.85	0.54
LSBC F571-V1	9.05	8.79 ± 0.05	2.77	0.54
LSBC F574-1	9.67	9.48 ± 0.03	3.16	0.65

Note. Only the first five galaxies are shown. The rest are in the electronic version.

(This table is available in its entirety in machine-readable form in the online article.)

point-by-point comparisons with kinematics and baryon density as a function of radius (see, for example, the radial acceleration relation; F. Lelli et al. 2017). A comparison between Spitzer and WISE stellar mass densities will provide a baseline for future work in this arena.

The subtle differences between the WISE W1 filter (centered at 3.4 μm) and the IRAC 3.6 μm filter (centered at 3.55 μm) are outlined in Paper I. Briefly, the two filters overlap for 87% of their flux with W1 having a longer blue side and IRAC 3.6 μm covering slightly more wavelength on the red side (see Figure 1 in Paper I). Both filters cover a known polycyclic aromatic hydrocarbon (PAH) feature at 3.3 μm, otherwise there are no strong emission line features in this part of a normal galaxy's SED.

On the Vega magnitude system, zero W1 − [3.6] colors are represented by a steep SED that falls off to the red. Galaxies with red, old stellar populations will have W1 − [3.6] colors near zero. Galaxies with notable star formation will have slightly more flux redward of the 3.3 μm PAH feature due to young AGB stars and contamination from hot dust redward of 4 μm. This produces slightly more flux in the IRAC 3.6 μm

filter than W1, resulting in slightly redder W1 − [3.6] colors. This also produces a reverse expectation from galaxy colors, where blue W1 − [3.6] colors signal old populations like ellipticals or spiral bulges, and red W1 − [3.6] colors signal star formation effects.

The SPARC sample is selected for rotational kinematics and covers all types of disk and dwarf galaxies with Hubble type Sa to Irr. As shown in Paper I, this produced a W1 − [3.6] color that was primarily on the red side of zero (between 0.15 and 0.25), where the mean elliptical color is 0.1 (see Figure 8 in Paper I). Low surface brightness (LSB) galaxies displayed slightly redder W1 − [3.6] colors than bright spirals. Comparison with stellar population models (J. M. Schombert & S. McGaugh 2014) indicates this is a combined SFR and metallicity effect with lower mean metallicity associated with low star formation and low stellar mass systems. Given the above trends in color, surface brightness, and mass, we anticipate weak W1 − [3.6] color gradients in spiral disks but, in general, the W1 flux should track the IRAC 3.6 μm flux.

All 175 galaxies in the original SPARC sample have WISE W1 images from the ALLWISE archive (F. Duey et al. 2023). However, a number of these galaxies have nearby stars or foreground galaxies which make quality reduction of the WISE images impractical. Of the original SPARC sample, we isolated 111 galaxies with good IRAC and W1 images. In addition, 81 of that subsample also have SDSS DR16 *ugri* images for optical comparison.

A subset of eight galaxies with SDSS *i*, W1, and IRAC 3.6 μm surface brightness profiles are shown in Figure 5. These eight galaxies were selected to cover a range of W1 − [3.6] colors, sizes, and profile shapes. Unsurprisingly, since their W1 − [3.6] colors are near zero, all the W1 and IRAC 3.6 μm profiles have nearly the same surface brightnesses (for clarity we interpolated the W1 radii to match the IRAC 3.6 μm radii). The exact same luminosity features seen in the IRAC 3.6 μm profiles are visible in the WISE W1 profiles. The W1 profiles were truncated when the surface brightness errors exceeded 0.25 mag arcsec^{-2}, which was due to a combination of lower S/N and greater uncertainty in the W1 sky value (sky uncertainty dominates photometry of galaxies over 1′ in size; see J. M. Schombert & S. McGaugh 2014).

The black lines in Figure 5 are the SDSS *i* surface brightness profiles shifted by a mean color of *i* − [3.6] = 2.5. The correspondence is excellent across all three filters with some expected deviation at large radii due to weak *i*-band color gradients. This gives some confidence to using far-IR photometry to follow the stellar mass in high-redshift samples. We note that the color–Υ_* relation for SDSS *i* has a factor of 5 larger dynamic range compared to W1 (see Figure 3 SML) with a proportionate amount of error in Υ_* for photometric errors in color. An optimal course of analysis would be to use higher-resolution optical imaging for local stellar mass determination tied to stellar mass values deduced from coarser, aperture near-IR values.

The conversion of surface brightness profiles into stellar mass density profiles is similar to the procedure for deducing total stellar masses (without the need for a galaxy distance as surface brightness is distance independent). As shown in Figure 6, three galaxies from the SPARC sample with varying morphological types and colors are selected for comparison of the IRAC 3.6 μm versus WISE W1 mass profiles. The model Υ_* value for each isophote is determined from either the

g − [3.6] or g − W1 color and applied to each radius independent of the surface brightness value in either W1 or 3.6 μm.

Again, the correspondence is excellent, regardless of the total stellar mass, where the IRAC 3.6 μm and WISE W1 values are in agreement within the observational errors (determined from the uncertainties in the photometry of each isophote). The WISE data were ignored below a 5″ radius due to the poor spatial resolution of the WISE imaging. Values below the point-spread function (PSF) will always reproduce lower mass density values as W1 flux will be distributed to a larger radius by the PSF. This results in larger uncertainties at higher surface densities for the WISE imaging in Figure 6. But the use of WISE W1 for the determination of stellar mass densities should be comparable to the mass models produced by Spitzer (F. Lelli et al. 2016), with the caveat of decreased spatial resolution from the larger PSF for WISE.

6. WISE Tully–Fisher Relation

The original form of the TF relation compared the H I line profile half-width velocity (W$_{50}$) versus stellar luminosity (typically for a filter in the red or near-IR to minimize extinction effects; M. Aaronson & J. Mould 1983). The link between gravitational mass and rotation is the underlying principle to the luminosity TF relation, where luminosity is a proxy for stellar mass. As the focus of many TF studies is rich clusters (see CosmicFlow; R. B. Tully et al. 2009), then the spirals studied are predominately early-type spirals. Cluster spirals are typically gas-poor and high-mass systems, ideally positioned for distance scale analysis as a class of objects.

The WISE luminosity TF relation is shown in Figure 7 for the SPARC sample with WISE W1 photometry and accurate distances. The sample is divided into two subsamples, those galaxies with redshift-independent distances and those galaxies with Hubble distances from the Extragalactic Distance Database (R. B. Tully et al. 2009). The top panel displays the absolute W1 total magnitudes determined from curves of growth as outlined in Paper I versus V_f, the asymptotic velocity value from the SPARC H I rotation curve (F. Lelli et al. 2019). The relationship is close to linear (in log space) with some indication of a change in slope at L_* ($M_{W1} = -22$).

A comparison to previous WISE TF fits is shown in Figure 7, using data from E. Kourkchi et al. (2020; Cosmic-Flows3) and R. Bell et al. (2023). Those studies focused on high-luminosity cluster spirals to map peculiar velocity in the local Universe and their fits agree on the high-luminosity end of our data. Deviations at the low-luminosity end are more than likely due to differences in photometric assignment to a total luminosity value for LSB dwarfs, and differences between rotation velocity from half-width velocities (W$_{50}$) and rotation curves (see F. Lelli et al. 2019).

The bottom panel of Figure 7 displays the stellar mass TF relationship. The key difference in this version of the TF relation is that W1 luminosity has been converted into stellar mass using the color prescriptions in Section 2. The stellar mass TF relation differs from the luminosity TF in that low-luminosity galaxies have bluer colors, and corresponding low Υ values. In addition, high-mass spirals have significant bulges, which have higher Υ values and a proportionally greater contribution to total stellar mass relative to their luminosities. This has the effect of raising the high-mass galaxies with
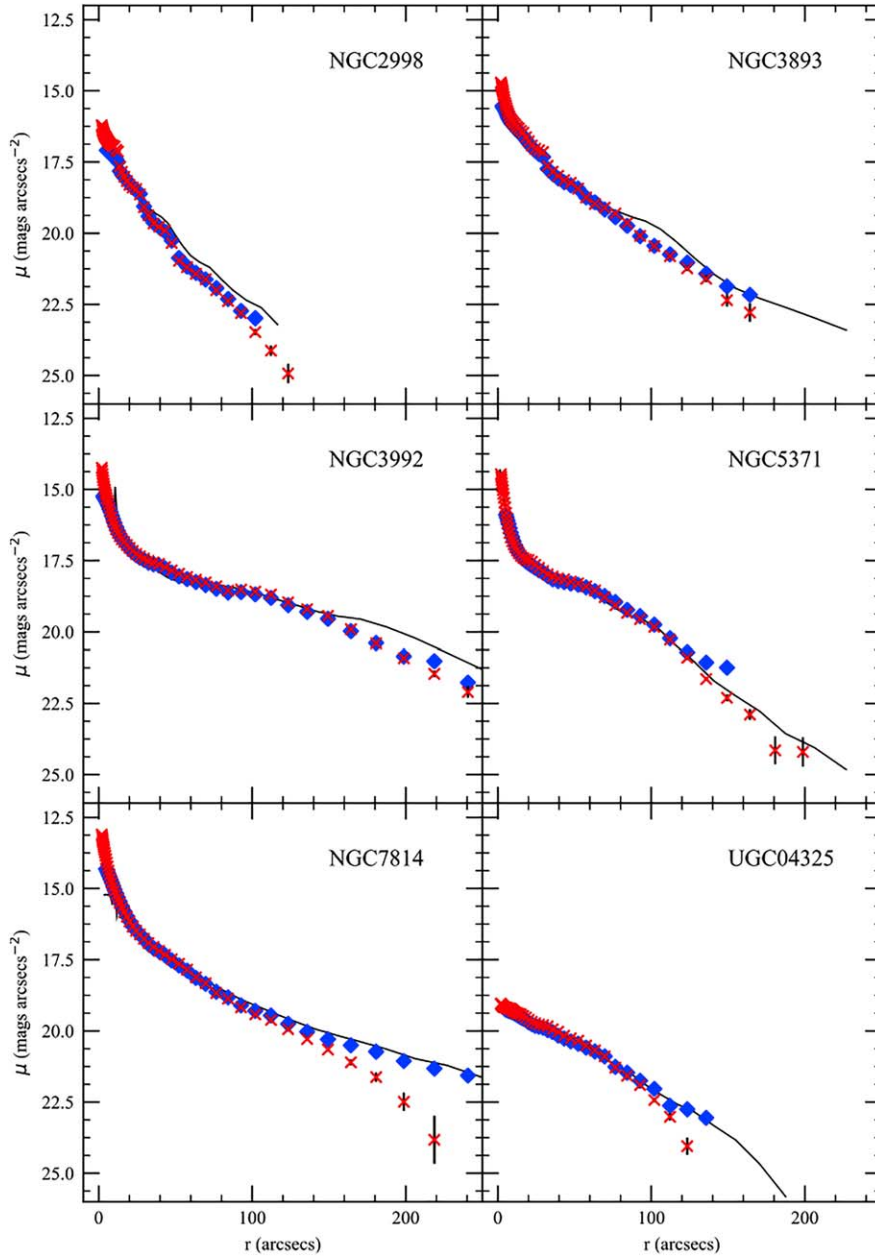
Figure 5. The WISE W1 surface brightness profiles (blue symbols) are compared to Spitzer IRAC 3.6 μm (red symbols) and SDSS i (black lines) profiles for six SPARC galaxies of varying mass, morphological type, and scale length. The W1 and 3.6 μm profiles are in excellent agreement with a small W1 − [3.6] color offset. All the same stellar luminosity features detected in 3.6 μm are seen in the W1 profiles. The SDSS i profiles are offset by an i − [3.6] = 2.5 color for comparison. The correspondence between the far-IR and near-IR is also excellent, providing additional confidence in the use of optical imaging to follow profiles to smaller radii where WISE imaging lacks resolution.

respect to the low-mass end, and improving the linearity of the entire correlation.

Also shown in the bottom panel of Figure 7 is the stellar mass fits from A. Ristea et al. (2024). For their study, stellar masses were assigned from MaNGA GALaxy Survey (K. Bundy et al. 2015) WISE photometry using the SED-fitting Code Investigating GALaxy Evolution algorithm (M. Boquien et al. 2019). Rotation velocities were determined for the stellar component (from Hα spectra) and the gas component (from H I spectra). The two different velocity measurements resulting in slightly different TF slopes as shown by the magenta area in Figure 7.

As with the luminosity TF, the stellar mass TF agrees well on the high-mass end, but overestimates the stellar masses (or underestimates the rotation velocity) on the low-mass end. As the SPARC data use the flat portion of the rotation curve, an underestimate is more likely. The linearity of stellar mass TF also breaks at approximately 10^{10} $M_\odot$, at the same luminosity as the luminosity TF deviates from linearity. This is also the point where the typical gas fraction rises about 20% for spirals indicating an increasing importance of the gas mass of a galaxy to its gravity and, thus, its rotation velocity.

7. Summary

Future work on deducing stellar masses from near-IR photometry will be less dependent on pointed observations from Spitzer (due to the recent end of mission) and more
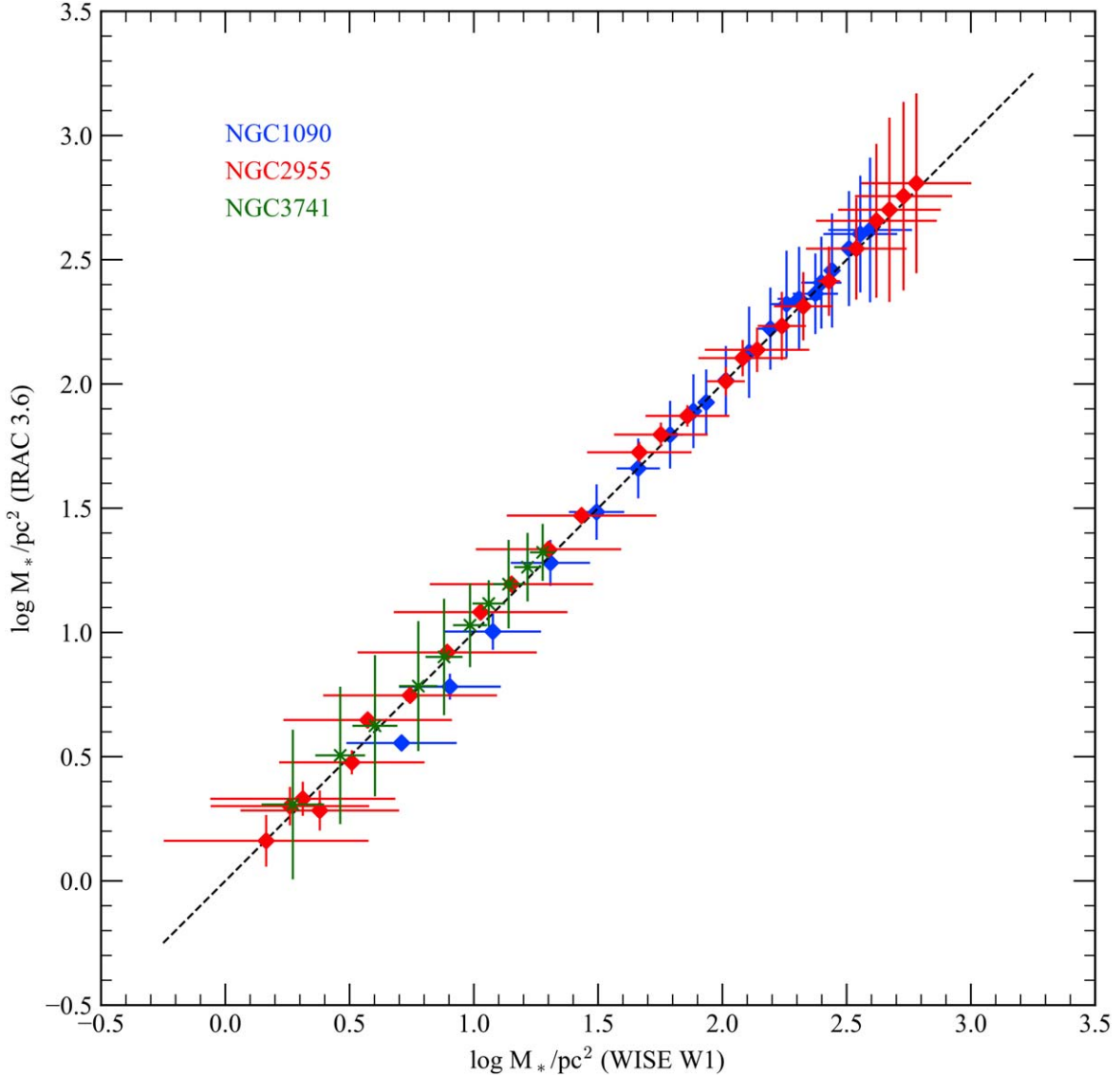
Figure 6. The comparison of three SPARC galaxy mass density profiles using WISE W1 surface brightness profiles vs. Spitzer IRAC 3.6 μm profiles.

dependent on all-sky surveys at similar wavelengths, such as the WISE mission. We present new stellar population models to produce simple, and effective, color–Υ_* relations at the WISE W1 wavelengths. Our main results are as follows.

1. We extend the stellar population models developed in J. Schombert et al. (2019) to cover the WISE filters. This is a simple interpolation from our previous models, empirically tied to the Spitzer IRAC 3.6 μm colors and calibrated to stellar cluster colors to correct for short-lived AGB populations inadequately addressed by isochrone studies.

2. Our color–Υ_* models follow three scenarios that cover the range of expected galaxy evolution. They are (a) a pure disk population, representing a slowly declining SFR history whose final strength is set by the main-sequence relation (J. S. Speagle et al. 2014) and a metallicity set by the current gas-phase metallicity (G. Cresci et al. 2019) with a chemical evolution scenario; (b) a pure bulge population composed of a passive, burst population that varies in color and Υ_* based on the color–metallicity relation (see SML); and (c)

a combined bulge + disk model that uses the well-known color–morphology relation to allow a user to estimate a mean Υ_* from total color or morphological type.

3. These three scenarios are shown graphically in Figure 1, where the most notable difference from the Spitzer color–Υ_* relation is an expected upward shift in Υ_* by approximately 0.1 dex. The dynamic range is nearly identical from IRAC 3.6 μm to WISE W1, meaning that similar photometric errors will reflect into similar errors in stellar mass for Spitzer versus WISE observations.

4. Stellar masses deduced from WISE photometry for the SPARC sample are in excellent agreement with our original stellar masses from Spitzer photometry and other WISE stellar masses in the literature (e.g., M. E. Cluver et al. 2014). This was not unexpected as the models are similar and the W1 to [3.6] colors are consistent with the 0.1 dex increase in Υ_* predicted by the population models.

5. Comparison with the S^{4}G survey stellar mass estimates (based on 3.6 μm aperture fluxes and the M. Eskew et al. 2012 models) plus the Dustpedia stellar masses (based on
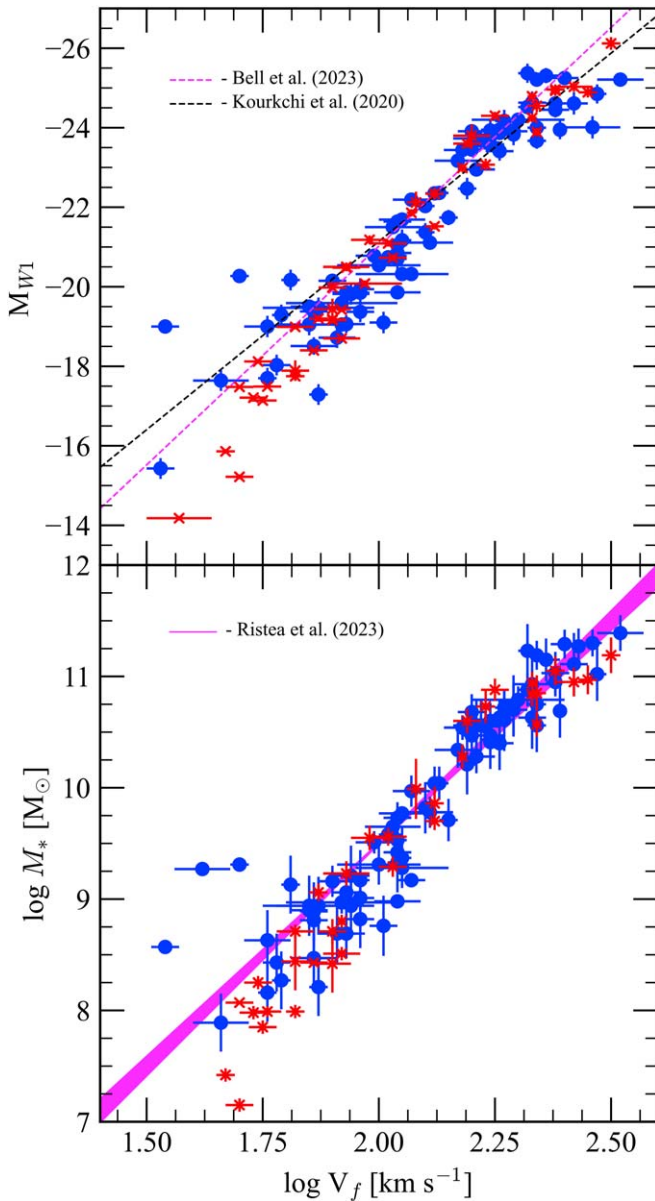
Figure 7. The luminosity and stellar mass TF relations for the SPARC WISE sample. Blue symbols indicate galaxies with Hubble flow distances, and red symbols are galaxies with redshift-independent distances (typical Cepheids or tip of the red giant branch estimates). The luminosity TF is key as a distance indicator. High-mass cluster spirals from E. Kourkchi et al. (2020) and R. Bell et al. (2023) are shown. The bottom panel displays the same data converted into stellar mass using the Υ values deduced as discussed in Section 2. For comparison, the stellar mass TF from A. Ristea et al. (2024) is shown. The range of fits for stellar vs. gas rotation curves is shown as the magenta band.

SED fits to 42 filters from GALEX to Planck) are also in excellent agreement with our W1 fluxes and our own stellar population scenarios. Comparison to other WISE and Spitzer studies reinforces the importance of using a galaxy color to confine the Υ_* models.

There are several takeaways from our new WISE W1 models and comparison to existing stellar mass estimates. First, the dynamic range in the color–Υ_* relations is still the smallest compared to optical filters, despite the uncertainties in the AGB component, and produces the most stable Υ_* values for the expected photometric errors. This is true both for integrated values (total galaxy stellar mass) and surface density profiles.

Second, varying SFHs are important for the low-mass, blue dwarf galaxies (at the 0.1 dex level), but to reproduce present-day galaxy colors, there is very little variation in Υ_* for high-mass, red spirals. Accuracy for early-type spirals is more dependent on separating the bulge and disk components (with their differing color–Υ_* relations) using moderately high-resolution surface photometry.

Third, the similar values between different data sets (e.g., S^{4}G) and different techniques (e.g., Dustpedia) indicate that the choice of filter set or modeling is less important than solid photometry data. It is encouraging that Υ_* values from the far-red to near-IR produce identical stellar mass values, as this region is less influenced by distortion due to extinction. This will also be critical in linking stellar mass estimates at high redshift (i.e., JWST) using UV and optical rest-frame photometry to present-day stellar mass deduced from near-IR fluxes. The full SED-fitting techniques of Dustpedia allow for a stable connection between those fluxes from deep-space imaging and near-IR calibrators.

Lastly, the differences between the luminosity TF and stellar mass TF are shown in Figure 7. The importance of the luminosity TF to distance scale work has been demonstrated in numerous studies (see R. B. Tully 2023 for a review). And the high-mass end has the smallest scatter since these systems have the smallest gas fractions and, therefore, the stellar mass represents the total baryon mass, which has the strongest correlation with rotational velocity (see F. Lelli et al. 2019). The conversion of luminosity to stellar mass (also shown in Figure 7) does not significantly improve the linearity of the TF relation, again due to the varying contribution of missing gas mass on the low-luminosity end, but does improve the shape of the high-mass end with the proper division of bulge versus disk Υ values and complete sum of the bulge and disk components.

Acknowledgments

ORCID iDs

Francis Duey https://orcid.org/0009-0003-1662-5179
James Schombert https://orcid.org/0000-0003-2022-1911
Stacy McGaugh https://orcid.org/0000-0002-9762-0980
Federico Lelli https://orcid.org/0000-0002-9024-9883

References

Aaronson, M., & Mould, J. 1983, ApJ, 265, 1
Baker, W. M., Maiolino, R., Belfiore, F., et al. 2023, MNRAS, 518, 4767
Bell, E. F., & de Jong, R. S. 2000, MNRAS, 312, 497
Bell, E. F., McIntosh, D. H., Katz, N., et al. 2003, ApJS, 149, 289
Bell, R., Said, K., Davis, T., et al. 2023, MNRAS, 519, 102
Boquien, M., Burgarella, D., Roehlly, Y., et al. 2019, A&A, 622, A103

Brown, M. J. I., Moustakas, J., Smith, J.-D. T., et al. 2014, ApJS, 212, 18
Bruzual, A. G. 1993, RMxAA, 26, 126
Bruzual, A. G. 2009, arXiv:0911.0791
Bruzual, G., & Charlot, S. 2003, MNRAS, 344, 1000
Bundy, K., Bershady, M. A., Law, D. R., et al. 2015, ApJ, 798, 7
Cassata, P., Guzzo, L., Franceschini, A., et al. 2007, ApJS, 172, 270
Clark, C. J. R., Verstocken, S., Bianchi, S., et al. 2018, A&A, 609, A37
Cluver, M. E., Jarrett, T. H., Hopkins, A. M., et al. 2014, ApJ, 782, 90
Conroy, C., & Gunn, J. E., 2010 FSPS: Flexible Stellar Population Synthesis, Astrophysics Source Code Library., ascl:1010.043
Consolandi, G., Gavazzi, G., Fumagalli, M., et al. 2016, A&A, 591, A38
Courteau, S. 1996, ApJS, 103, 363
Cresci, G., Mannucci, F., & Curti, M. 2019, A&A, 627, A42
de Vaucouleurs, G., de Vaucouleurs, A., Corwin, H. G., et al. 1991, Third Reference Catalogue of Bright Galaxies (New York: Springer)
Duey, F., Tosi, S., & Schombert, J. 2023, AAS Meeting, 241, 403.05
Dressler, A., Vulcani, B., Treu, T., et al. 2023, ApJL, 947, L27
Driver, S. P., , GAMA Team, Baldry, I. K., et al. 2009, in IAU Symp. 254, The Galaxy Disk in Cosmological Context, ed. J. Andersen, J. Bland-Hawthorn, & B. Nordström (Cambridge: Cambridge Univ. Press), 469
Eggen, O. J., Lynden-Bell, D., & Sandage, A. R. 1962, ApJ, 136, 748
Eskew, M., Zaritsky, D., & Meidt, S. 2012, AJ, 143, 139
Gallazzi, A., & Bell, E. F. 2009, ApJS, 185, 253
Gallazzi, A., Charlot, S., Brinchmann, J., et al. 2005, MNRAS, 362, 41
Gallazzi, A., Charlot, S., Brinchmann, J., et al. 2006, MNRAS, 370, 1106
Gonzalez-Perez, V., Lacey, C. G., Baugh, C. M., et al. 2014, MNRAS, 439, 264
Graham, A. W., & Worley, C. C. 2008, MNRAS, 388, 1708
Hogg, D. W. 2022, arXiv:2206.00989
Hosek, M. W., Lu, J. R., Lam, C. Y., et al. 2020, AJ, 160, 143
Ibarra-Medel, H. J., Avila-Reese, V., Lacerna, I., et al. 2022, MNRAS, 510, 5676
Jarrett, T. H., Cluver, M. E., Taylor, E. N., et al. 2023, ApJ, 946, 95
Jarrett, T. H., Cluver, M. E., Brown, M. J., et al. 2019, ApJS, 245, 25
Lee, J. H., Pak, M., Jeong, H., et al. 2023, MNRAS, 521, 4207
Korsaga, M., Famaey, B., Freundlich, J., et al. 2023, ApJL, 952, L41
Kourkchi, E., Courtois, H. M., Graziani, R., et al. 2020, AJ, 159, 67
Lelli, F., McGaugh, S. S., & Schombert, J. M. 2016, AJ, 152, 157
Lelli, F., McGaugh, S. S., Schombert, J. M., et al. 2017, ApJ, 836, 152
Lelli, F., McGaugh, S. S., Schombert, J. M., et al. 2019, MNRAS, 484, 3267
Lin, C. C., & Shu, F. H. 1964, ApJ, 140, 646
Maraston, C. 2005, MNRAS, 362, 799
McGaugh, S. S., & Schombert, J. M. 2014, AJ, 148, 77
McGaugh, S. S., Schombert, J. M., & Lelli, F. 2017, ApJ, 851, 22
Meidt, S. E., Schinnerer, E., van de Ven, G., et al. 2014, ApJ, 788, 144
Muñoz-Mateos, J. C., Sheth, K., Regan, M., et al. 2015, ApJS, 219, 3
Prantzos, N. 2009, in IAU Symp. 254, The Galaxy Disk in Cosmological Context, ed. J. Andersen, J. Bland-Hawthorn, & B. Nordström (Cambridge: Cambridge Univ. Press), 318
Rakos, K. D., & Schombert, J. M. 1995, ApJ, 439, 47
Ristea, A., Cortese, L., Fraser-McKelvie, A., et al. 2024, MNRAS, 527, 7438
Robotham, A. S. G., Bellstedt, S., Lagos, C. D. P., et al. 2020, MNRAS, 495, 905
Roth, M. M., Madhav, K., Stoll, A., et al. 2023, Proc. SPIE, 12424, 124240B
Salaris, M., Weiss, A., Cassarà, L. P., et al. 2014, A&A, 565, A9
Schombert, J., McGaugh, S., & Lelli, F. 2019, MNRAS, 483, 1496
Schombert, J., McGaugh, S., & Lelli, F. 2022, AJ, 163, 154
Schombert, J. M. 2016, AJ, 152, 214
Schombert, J. M., & McGaugh, S. 2014, PASA, 31, e011
Sheth, K., Regan, M., Hinz, J. L., et al. 2010, PASP, 122, 1397
Speagle, J. S., Steinhardt, C. L., Capak, P. L., et al. 2014, ApJS, 214, 15
Strateva, I., Ivezić, Ž., Knapp, G. R., et al. 2001, AJ, 122, 1861
Taylor, E. N., Hopkins, A. M., Baldry, I. K., et al. 2011, MNRAS, 418, 1587
Tinsley, B. M. 1968, ApJ, 151, 547
Tinsley, B. M. 1978, in IAU Symp. 80, The HR Diagram: The 100th Anniversary of Henry Norris Russell, ed. A. G. Davis Philip & D. S. Hayes (Dordrecht: Reidel), 247
Tinsley, B. M. 1980, FCPh, 5, 287
Trager, S. C., Worthey, G., Faber, S. M., et al. 1998, ApJS, 116, 1
Treu, T., Ellis, R. S., Liao, T. X., et al. 2005, ApJ, 633, 174
Tully, R. B. 2023, arXiv:2305.11950
Tully, R. B., Rizzi, L., Shaya, E. J., et al. 2009, AJ, 138, 323
Villaume, A., Conroy, C., & Johnson, B. D. 2015, ApJ, 806, 82
Walcher, J., Groves, B., Budavári, T., et al. 2011, Ap&SS, 331, 1
Weisz, D. R., Dalcanton, J. J., Williams, B. F., et al. 2011, ApJ, 739, 5
Werner, M. W., Roellig, T. L., Low, F. J., et al. 2004, ApJS, 154, 1
Willmer, C. N. A. 2018, ApJS, 236, 47
Wright, E. L., Eisenhardt, P. R. M., Mainzer, A. K., et al. 2010, AJ, 140, 1868